

Direct Laser Writing of Ferromagnetic Nickel Utilizing the Principle of Sensitized Triplet-Triplet Annihilation Upconversion

Kristin E. J. Kühl,^{*,†} Katharina Rediger,[‡] Nikhita Khera,[†] Ephraim Spindler,[†]
Gereon Niedner-Schatteburg,[‡] Elke Neu,[†] Mathias Weiler,[†] and Georg von
Freyermann^{†,¶}

[†]*Department of Physics and Research Center OPTIMAS, RPTU University
Kaiserslautern-Landau, 67663 Kaiserslautern, Germany*

[‡]*Department of Chemistry, RPTU University Kaiserslautern-Landau, 67663
Kaiserslautern, Germany*

[¶]*Fraunhofer Institute for Industrial Mathematics ITWM, 67663 Kaiserslautern, Germany*

E-mail: kuehlik@rptu.de

Abstract

Direct laser writing of ferromagnetic microstructures is of great interest for sensing and data storage in compact three-dimensional architectures. However, reliable direct laser writing of metallic and even more so ferromagnetic materials remains a major challenge. Here, we present a novel photoresist suitable to direct laser write ferromagnetic nickel based on sensitized triplet-triplet annihilation upconversion. By combining an in-situ photochemical deoxygenation process with a sensitized triplet-triplet annihilation upconversion process as well as a photoreduction of Ni²⁺ ions, the deposition of metallic nickel is enabled under ambient conditions. Using this approach, nickel structures are fabricated as a proof of concept. Scanning electron microscopy and EDX analysis confirm the spatially confined deposition of nickel, while magnetic characterization by vibrating sample magnetometry and scanning NV magnetometry demonstrate the ferromagnetic nature of the printed structures. This work presents a major step forward in extending the possibilities of direct laser writing to metallic and ferromagnetic materials.

Abbreviations

2PA two-photon absorption

DIPEA diisopropylethylamine

DLW Direct Laser Writing

DMF 2,5-dimethylfuran

DMI 1,3-Dimethyl-2-imidazolidinone

EDX energy dispersive X-ray spectroscopy

ESR electron spin resonance

NV nitrogen vacancy

ODMR optically detected magnetic resonance

PTOEP platinum octaethylporphyrin

SCE saturated calomel electrode

sTTA-UC sensitized triplet-triplet annihilation upconversion

TTET triplet triplet energy transfer

Keywords

Microstructures, Direct Laser Writing, Photochemical Deoxygenation, Sensitized Triplet-Triplet Annihilation Upconversion, Photoredox Catalysis, Nitrogen-Vacancy-Magnetometry, Ferromagnetism

Introduction

Complex three-dimensional microstructures are attracting increasing interest in science and technology and promise the realization of a wide variety of applications extending from the field of plasmonics¹⁻⁴ through aviation and automotive industries^{5,6} to biotechnology and medicine.⁶⁻⁸ While applications so far rely mainly on polymeric and ceramic hybrid materials, manufacturing such structures from metals and especially from non-noble metals, continues to challenge scientists.

Direct laser writing (DLW) is a versatile method for additive manufacturing of microscale polymeric structures.^{9,10} Until now, there exists only a limited number of proposals to fabricate metallic structures using DLW. In 2006 Tanaka *et al.* reported fabrication of gold and silver structures from aqueous solutions of HAuCl_4 and AgNO_3 .¹¹ Over the course of time structural quality improved: Blasco *et al.* fabricated conductive gold-containing composite structures by simultaneous photopolymerization of an acrylate-functionalized poly(ethylene glycol) derivative and photoreduction of HAuCl_4 ¹² and Waller *et al.* demonstrated highly conductive silver structures from a gelatin containing aqueous solution of AgClO_4 .¹³ However, those methods are focused on noble metals, which are useful for highly conducting structures requested, *e.g.* in plasmonic applications. Applications like microelectronic devices such as sensors and actuators¹⁴ or fully motion-controlled microrobots¹⁵ would benefit from the possibility of printing ferromagnetic materials. However, due to their lower standard potentials, which corresponds to a smaller thermodynamic driving force for electron uptake,¹⁶ such non-noble metals are more

difficult to deposit from solutions, which calls for more complex processes to enable manufacturing using DLW.

Typically, DLW utilizes a two-photon absorption (2PA) process to initiate the photoreaction inside a very small volume defined by the iso-intensity surface of a tightly focused laser beam. This volume is often called voxel, short for volume pixel, and often has a lateral diameter lower than 100 nm and an axial extension of approximately 300 nm, depending on parameters such as laser power.¹⁷ The photoreaction is confined to this volume only due to a nonlinear (mostly quadratic) relationship between laser intensity and the polymerization threshold.^{9,10} While 2PA inherently provides this nonlinearity, current research also addresses other multiphoton processes to provide a nonlinearity for the printing process. Hahn *et al.* used consecutive two-step absorption instead of simultaneous 2PA.¹⁸ Awwad *et al.* and Z. Wang *et al.* induced polymerization *via* sensitized triplet-triplet annihilation upconversion (sTTA-UC).^{19,20} This approach exploits the conversion of two low-energy excitations into a high-energy excitation. In this way, the use of expensive femtosecond pulsed lasers can be avoided while maintaining a quadratic dependence of the concentration of the printing-relevant excited states on the incident light intensity.

Y. Wang *et al.* used two-photon decomposition of metal carbonyls in combination with optical force trapping and sintering with the printing laser to print molybdenum, cobalt and tungsten structures. This trapping and sintering process is enhanced by the localized surface plasmon resonance the laser excites in the metal nanoparticles.²¹ With this technique, they achieved writing speeds of up to $20 \mu\text{m s}^{-1}$.²¹ However, their resist needs to be prepared in a glove box under inert atmosphere and sealed in a liquid cell to shield it from oxygen, which would quench the process.

In this work, we present a new approach to DLW of nickel utilizing a sTTA-UC process to initiate the photoreduction of nickel ions by a sacrificial electron donor in combination with *in situ* deoxygenation. This introduces active

protection of triplet states by incorporating an oxygen scavenger within the system,²² which increases the writing speed up to $100 \mu\text{m s}^{-1}$.

Results and Discussion

Underlying photochemical reactions

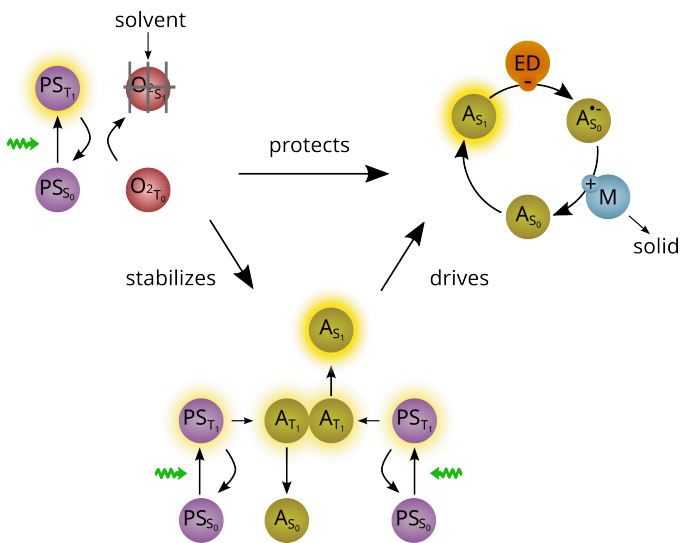


Figure 1: Graphical representation of the cooperating chemical processes. The fundamental process is the photochemical deoxygenation performed by excitation of the photosensitizer (PS), generating singlet state oxygen (O_{2S_1}) by energy transfer. The excited state of molecules is symbolized by a yellow halo. This O_{2S_1} is permanently removed by oxidation of the solvent, symbolized by bars (left part). This provides a local deoxygenated volume which enables a sTTA-UC process generating the annihilator (A) in its first excited singlet state S_1 . The annihilator S_1 enables the photoreduction of metal ions into neutral atoms that precipitate into bulk metal (M) *via* electron transfer by an electron donor (ED) (right part).

We combine three photochemical processes, a graphical representation of which is displayed in Fig. 1. All processes are running in parallel. In a first process, the surrounding solvent is locally deoxygenated: the photosensitizer singlet PS_{S_0} is excited into its triplet state PS_{T_1} , which is quenched through energy transfer to the dissolved O_{2T_0} , generating singlet state oxygen

O_{2S_1} . O_{2S_1} molecules are then permanently removed from the solution by a reaction with the molecules of the surrounding solvent that serves as oxygen scavenger. These locally oxygen-free conditions enable a second process: sTTA-UC excites the annihilator to its singlet state A_{S_1} required for following the redox reaction. In this third process, the annihilator in the S_1 state generated by sTTA-UC is quenched by electron transfer from a sacrificial electron donor (ED) to the annihilator. The thus reduced annihilator proliferates its extra electron to the nickel cation. As an alternative pathway, the excited annihilator A_{S_1} could transfer energy to the nickel cation, which is then subsequently reduced by the electron donor. Either of both pathways would need to take place twice in order to generate nickel⁽⁰⁾.

As sTTA-UC is not very well established in the DLW community, we depict the principle in Fig. 2 in greater detail. In the first step, a 532 nm continuous wave laser excites a photosensitizer to its first excited singlet state S_1 , which is converted to the T_1 triplet state *via* intersystem crossing. This is followed by a triplet-triplet energy transfer (TTET) from the triplet state of the photosensitizer to the triplet state of the annihilator. Two annihilator molecules in the T_1 state may undergo triplet-triplet annihilation by an upconversion process that transforms one of the two in the ground state S_0 and one in the excited state S_1 .^{23,24} Due to the reaction of two sensitizer molecules, sTTA-UC realizes the required nonlinearity for the DLW process.²⁰

Implementation of the specified processes in the resist

Table 1: The employed compounds and their proposed function

Compound	Function in the resist
Erythrosine B	photosensitizer
perylene	annihilator
DIPEA	sacrificial electron donor
$\text{NiCl}_2 \cdot 6\text{H}_2\text{O}$	supplier of nickel ²⁺ cations
DMI	deoxygenating solvent

After this schematic description of the underlying mechanism, we will now investigate the experimental realization of the various processes. The used compounds and their proposed functions in the resist can be found in Table 1. Various studies have shown that efficient sTTA-UC processes are usually limited to oxygen-free environments since the triplet ground state of molecular oxygen acts as a quencher for the employed triplet states.^{25,26} However, efficient sTTA-UC in aerated solutions is achieved by deoxygenating solvents which are binding molecular singlet oxygen, which is formed from the triplet state by the excited sensitizer in the first process.^{27,28} Here, 1,3-Dimethyl-2-imidazolidinone (DMI) is used for this purpose²⁷ and the deoxygenating properties are verified using the oxygen sensitive phosphorescence of platinum octaethylporphyrin (PTOEP) as established by Wan *et al.*²⁷ before. Upon continuous irradiation ($\lambda = 532$ nm) the integrated phosphorescence intensity of a solution of 10×10^{-5} M PTOEP in DMI increased by more than 43-fold within 5 min of irradiation time (Fig. S1). UV/vis absorption spectra recorded before and after irradiation exhibited no observable changes, indicating that the concentration of PTOEP was unaffected by the irradiation. Additionally, the excited state lifetime increased from (670 ± 6) ns (Fig. S2) before excitation to (1746 ± 13) ns (Fig. S3) after 5 min, confirming the decreasing oxygen concentration in solution further. Thus, DMI was chosen as a deoxygenating solvent for the photoresist. The sensitizer 2-(6-hydroxy-2,4,5,7-tetraiodo-3-oxoxanthen-9-yl)benzoic acid (Erythrosine B) used in the sTTA-UC process also serves as a sensitizer for generating singlet oxygen.²⁹

Due to the *in situ* establishment of an oxygen-free local environment, the sTTA-UC process is enabled to operate efficiently. For this purpose, Erythrosine B was used as sensitizer, since the energy of the donating T_1 state ($E_{T_1}(\text{Erythrosine B}) = 1.89$ eV)³¹ is sufficiently higher than the T_1 energy of the used annihilator perylene (per) ($E_{T_1}(\text{per}) = 1.53$ eV),³² thus enabling an efficient TTET to take place.^{23,24} Also, the excited singlet state

of perylene ($E_{S_1}(\text{per}) = 2.76$ eV)³² can be populated upon recombining two triplet molecules $E_{T_1}(\text{per})$, which is a fundamental requirement for a triplet-triplet annihilation upconversion process.^{23,24} Thus, we check Erythrosine B and 100 eq. perylene in DMI mixture for luminescence of the upconverted S_1 state and weak upconverted emission was found with a maximum at 474 nm (Fig. S4). However, it is suggested that the intensity is predominantly attenuated by reabsorption effects of the photosensitizer in the solution. The perylene molecule is in its excited S_1 state once the sTTA-UC takes place, from where it is able to start the photocatalytic reduction of nickel. The Erythrosine B molecule relaxes back to its ground state, ready to act as a photosensitizer again.

The photochemical reduction of nickel is carried out using the upconverted annihilator perylene as a photocatalyst, diisopropylethylamine (DIPEA) as a sacrificial electron donor and nickel(II) chloride hexahydrate ($\text{NiCl}_2 \cdot 6\text{H}_2\text{O}$) as a metal compound that supplies the reaction with nickel²⁺ cations. Starting with the perylene in the excited S_1 state ($E_{S_1}(\text{per}) = 2.76$ eV),³² generated by sTTA-UC, the metallic nickel⁽⁰⁾ can be formed by two different redox pathways (Fig. 3). To estimate, which mechanism could play a dominating role, the excited state redox potentials of perylene are considered. The excited state reduction potential of perylene in the S_1 state is approximated as³³

$$E(\text{per})_{\text{red}}^* = E(\text{per})_{1/2}^{\text{red}} + E(\text{per})_{0,0} \quad (1)$$

where $E(\text{per})_{\text{red}}^*$ refers to the excited state reduction potential, $E(\text{per})_{1/2}^{\text{red}}$ to the ground state reduction potential of the photocatalyst and $E(\text{per})_{0,0}$ to the excited state energy approximated as $E_{S_1}(\text{per})$. The perylene used in the resist exhibits ground state reduction potentials of $E_{\text{red}}(\text{per}) = -1.67$ V (per + $1e^- \rightleftharpoons \text{per}^{\bullet-}$) vs. saturated calomel electrode (SCE) in DMF³⁴ and $E_{\text{red}}(\text{per}^+) = 0.85$ V (per ^{$\bullet+$} + $1e^- \rightleftharpoons \text{per}$) vs. SCE in acetonitrile.³⁴ Thus, the excited state reduction potentials of perylene are calculated as $E_{\text{red}}(\text{per}^*) = 1.09$ V (per + $1e^- \rightleftharpoons \text{per}^{\bullet-}$) and $E_{\text{red}}(\text{per}^{+*}) = 3.61$ V (per ^{$\bullet+$} + $1e^- \rightleftharpoons \text{per}$) respectively. For

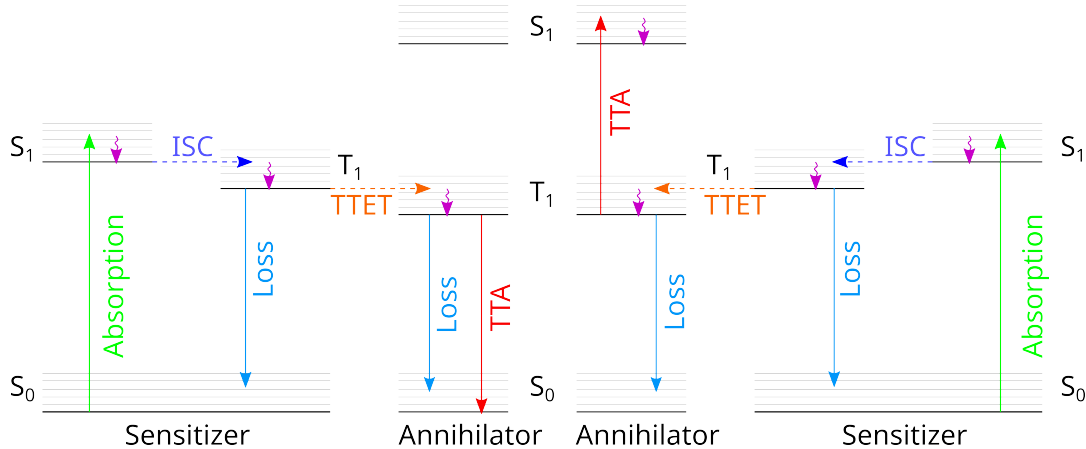


Figure 2: Energy level diagram showing the steps of the triplet-triplet annihilation upconversion process. First, light gets absorbed by the sensitizer (green arrow). After internal conversion and vibrational relaxation (pink arrow) to its first singlet state, the triplet state T_1 is formed *via* intersystem crossing (dashed dark blue arrow). Next, TTET occurs between the emitter and sensitizer (dashed orange arrow). When two annihilator molecules in the T_1 state collide, triplet-triplet annihilation upconversion occurs exciting one molecule to a higher energy singlet state with the second relaxing to the ground state (red arrows). The bright blue arrows represent potential non-radiative decay during the process of sTTA-UC. Adapted from.³⁰

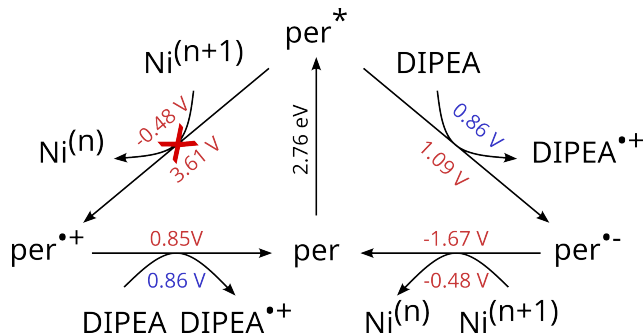


Figure 3: Latimer diagram of a photocatalytic reduction of nickel ions by perylene (per) with DIPEA as an electron donor. The central vertical arrow indicates excitation of perylene to the S_1 state with the corresponding excitation energy. Apart from this one, each arrow represents a redox half-reaction between two adjacent oxidation states. Red numbers indicate reduction and blue numbers oxidation potentials, both referenced to SCE. Electron transfer is thermodynamically favorable when the reduction potential of the acceptor exceeds that of the donor. For the electron donor DIPEA, the oxidation potential is given. For consistency, it is converted to the corresponding reduction potential (*i.e.* with inverted sign) when evaluating the energy balance.

the reductive half reaction (Fig. 3, right side), the excited state reduction potential of perylene ($E_{\text{red}}(\text{per}^*) = 1.09 \text{ V}$ ($\text{per} + 1e^- \rightleftharpoons \text{per}^{\bullet-}$)) is compared to the oxidation potential of the electron donor DIPEA ($E_{\text{ox}}(\text{DIPEA}) = 0.86 \text{ V}$ ($\text{DIPEA} \rightleftharpoons \text{DIPEA}^{\bullet+} + 1e^-$) vs. SCE in DCM),³⁵ leading to the suggestion of the reaction taking place. With a reduction potential of $E_{\text{red}}(\text{Ni}) = -0.48 \text{ V}$ ($\text{Ni}^{2+} + 2e^- \rightleftharpoons \text{Ni}^0$) vs. SCE¹⁶ of the nickel compound, the reduced perylene radical anion is able to reduce the nickel cations to metallic nickel. Since the oxidation state of the nickel ions from $\text{NiCl}_2 \cdot 6\text{H}_2\text{O}$ is two, two sacrificial electron donor molecules are needed to form the bulk metal $\text{Ni}^{(0)}$.

For the oxidative half-reaction pathway to take place (Fig. 3, left side), the excited state reduction potential of perylene ($E_{\text{red}}(\text{per}^{\bullet+}) = 3.61 \text{ V}$ ($\text{per}^{\bullet+} + 1e^- \rightleftharpoons \text{per}^*$)) is compared to the reduction potential of the nickel pair ($E_{\text{red}}(\text{Ni}) = -0.48 \text{ V}$ ($\text{Ni}^{2+} + 2e^- \rightleftharpoons \text{Ni}^0$) vs. SCE).¹⁶ However, this reaction pathway is revealed to be hindered by the strongly oxidative potential of the perylene radical cation, which would be formed during this reaction. Thus, the oxidative pathway is considered as strongly suppressed. Alternatively, energy transfer from the perylene S_1 state to the Ni^{2+} could be sug-

gested, but is suppressed due to selection rules since aqueous Ni^{2+} has a triplet ground state.³⁶

To further investigate the reductive pathway, the quenching mechanism was evaluated by Stern-Volmer measurements (Fig. S5). The quenching constant of $k_q^{\text{DIPEA}} = (2.24 \pm 0.03) \times 10^9 \text{ M}^{-1} \text{ s}^{-1}$ for perylene being quenched by DIPEA suggests a dominantly diffusion-controlled mechanism. Thus, the concentration of the electron donor DIPEA could significantly influence the efficiency of the DLW process.

A sketch of the DLW setup as well as further details can be found in a previous paper³⁷ and in the Methods section. The photoresist is freshly prepared before each application to ensure that its composition remained unchanged. Details of the photoresist can be found in the Methods section. For application in the DLW system, a glass substrate is sputtered with a 3 nm thin transparent layer of iridium. Iridium has strong spin-orbit coupling due to heavy atom effect and thus enhances the intersystem-crossing to the triplet states required for sTTA-UC.³⁸ The photoresist is sandwiched between the coated substrate and a glass window using tape as a spacer. To avoid evaporation of the resist the cell is sealed using Marabu Fixogum, a commercially available adhesive (for further details see the Methods section).

The power of the laser is adjusted to provide 15 mW power at the entrance pupil of the microscope objective at 100% printing power. For most printing processes, the power is tuned down to 60% to 80%. The scan speed for printing of the structures in Fig. 4 is $100 \mu\text{m s}^{-1}$. We observe a slight degradation of the printing efficiency after 60 min, which is most probably due to consumption of Ni^{2+} ions.

After exposure the substrate is dipped into acetone for 2 min and isopropyl alcohol for 1 min to dissolve the remaining resist and reveal the printed structures. Finally, the substrate is dried using a flow of gaseous nitrogen.

Direct Laser Written Nickel structures and their properties

As a proof of concept, we print 2.5D nickel structures. Fig. 4 a) and b) show exemplary

SEM images of printed structures. Fig. 4 c) displays the spatial distribution of nickel obtained by energy dispersive X-ray spectroscopy (EDX), matching the area displayed in Fig. 4 b). It is clearly recognizable that nickel is detected where the printed material is deposited. Besides some less densely distributed carbon, most likely resulting from heat generation in the laser focus, all other elements that could be detected by EDX are detected equally over the whole area, or even more at the area without the structures, and thus appear to be components of the substrate. All countmaps of elements that EDX was able to detect in the sample are shown in Fig. S6.

To determine the material density of the printed structures, cross-sections from a printed structure are prepared using a focused ion beam to sequentially slice the sample. An SEM image is taken for each slice during the cross sectioning. Fig. 4 d) shows one of the SEM images with a side view onto the surface, on which pores with a diameter of about 50 nm to 200 nm are visible. The images were analyzed with a graphics processing software. The density of the printed material is found to be $(96 \pm 3) \%$.

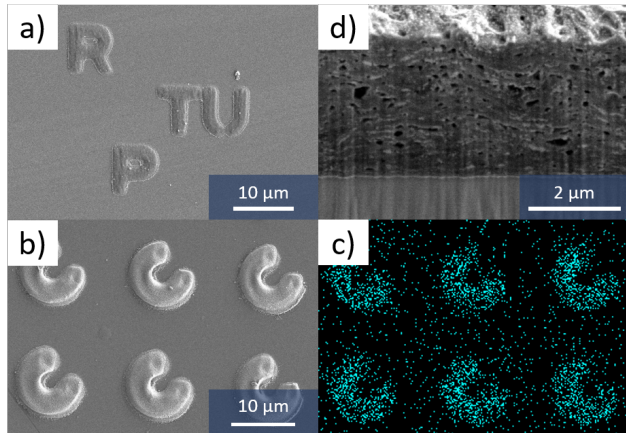


Figure 4: SEM images of 2.5D nickel structures printed using the proposed resist. a) Our university’s logo. b) A close up of an array of ring segments. c) EDX obtained countmap visualizing the distribution of nickel matched to the sample area in b). d) Cross section of a structure generated using a focused ion beam.

Ferromagnetic characteristics of the printed structures

To evaluate the magnetic properties of the printed nickel structures, we first performed vibrating sample magnetometry on an array of microdots (diameter $\approx 10\ \mu\text{m}$, height $\approx 0.6\ \mu\text{m}$). The magnetic moment was recorded for both decreasing (Direction 1, orange) and increasing (Direction 2, blue) external fields $\mu_0 H_{\text{ext}}$ after initial saturation at $\pm 9\ \text{T}$, respectively. We calculated the magnetization from the measured moment and sample volume obtained from confocal microscopy as described in the Methods section. Fig. 5a) displays the corresponding hysteresis loop. The obtained saturation magnetization of $M_S = (486 \pm 91)\ \text{kA m}^{-1}$ agrees with the literature value of $480\ \text{kA m}^{-1}$.³⁹ The uncertainty of our value M_S is primarily dominated by the determination of the microdot array volume via confocal microscopy. The resulting loop exhibits a saturation field of approximately 200 mT and a remanence of about 11% of M_S . These values are significantly higher than those of bulk nickel, which typically saturates at fields below 1 mT and exhibits negligible remanence at room temperature.⁴⁰ While a direct comparison to bulk material neglects the demagnetizing effects inherent to microstructures, micromagnetic simulations for an ideal cylindrical nickel dot (10 μm diameter, 0.6 μm height) predict a saturation field ($M \geq 0.95 \cdot M_S$) of only 50 mT. This discrepancy suggests pronounced domain wall pinning, likely originating from the internal structure of the printed material, specifically the gaps and cavities visible in the cross-section in Fig. 4c).

Nitrogen-vacancy magnetometry

To investigate the magnetic properties of individual structures, we employ a commercial scanning NV setup (ProteusQ, Qnami, see Methods section for further details), allowing to quantitatively measure the magnetic stray field above the sample (Fig. 5b). The measured nickel disc is prepared in its remanent state. The sample was saturated with an in-plane field

of approximately 300 mT and the NV probe was scanned at a lift height of 500 nm, using only a weak bias field to spectrally separate the NV spin resonances. The resulting map of the longitudinal field projection $\mu_0 H_{\text{NV}\parallel}$ is shown in Fig. 5c), revealing pronounced stray-field contrast and ferromagnetic ordering of the printed nickel. The stray-field modulation spans the entire microdot without significant internal fluctuations, indicating that the detected dipolar field originates from the macroscopic remanent magnetization of the structure. By comparing the experimental data with the calculated dipolar field of a fully saturated dot ($\approx 60\ \text{mT}$), we estimate the remanence of this specific structure to be 1% to 2% (see Fig. S7). This value is notably lower than the 11% average remanence determined *via* VSM for the microdot array.

The absence of resolvable magnetic domain contrast in the stray-field image can be attributed to two factors. First, a characteristic domain size below 500 nm would lead to a rapid decay of the field modulation with increasing distance from the surface. Consequently, such domains would remain unresolved at the given probe-to-sample distance. The formation of small domains is likely promoted by the internal morphology of the material, where cavities act as pinning sites or locally break the exchange coupling—the fundamental interaction that maintains long-range ferromagnetic alignment—thereby favoring a reduction in the characteristic magnetic length scales.

Second, a layered growth process may favor an antiferromagnetic-like coupling between consecutive layers, as the aforementioned cavities predominantly reside at the interfaces between printed layers. These may partially decouple the magnetic moments of adjacent layers whereas intra-layer exchange coupling remains largely undisturbed. This could result in a lamellar structure with compensated magnetization directions, leading to a high degree of magnetic flux closure within the dot.

Conclusions

A new photochemical strategy for direct laser writing of metallic material was introduced, ad-

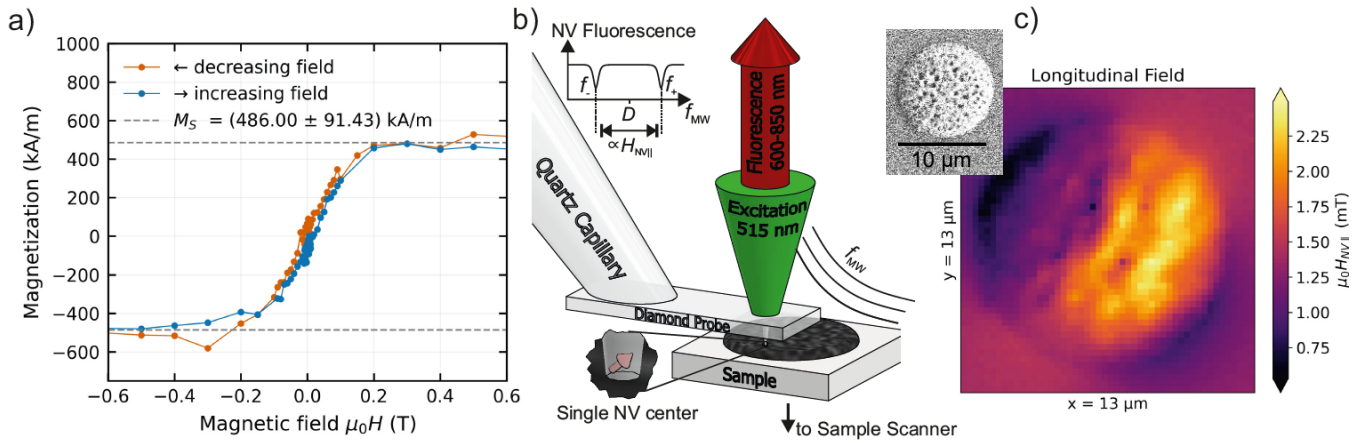


Figure 5: Magnetic characterization of nickel microdots. a) Room-temperature magnetic hysteresis loop of a nickel dot array of elements analogous to the structure shown in c. b) Schematic of the scanning NV magnetometer utilized for single-structure characterization. The upper-left inset schematically displays an optically detected magnetic resonance (ODMR) spectrum, where the resonances f_- ($m_S = 0 \leftrightarrow m_S = -1$) and f_+ ($m_S = 0 \leftrightarrow m_S = +1$) of the NV electronic ground state are visible. Within the small-field approximation, the Zeeman splitting around the zero-field splitting D is proportional to the magnetic field projection onto the NV quantization axis, $\mu_0 H_{\text{NV}\parallel}$. c) Top left: SEM image of the investigated microdot. The main panel shows the quantitative stray field map ($\mu_0 H_{\text{NV}\parallel}$) recorded scanning the NV at a height of 500 nm above the nickel structure. The structure was saturated at 300 mT and measured in remanence, using a small bias field to ensure clear splitting of the NV resonances.

addressing key limitations in the additive manufacturing of ferromagnetic metals. By combining photochemical deoxygenation, sensitized triplet-triplet annihilation upconversion, and photoredox-catalyzed metal reduction, a stable DLW process for Nickel was realized under ambient conditions using a continuous wave 532 nm excitation.

Nickel structures were fabricated with the proposed photoresist as proof of concept, exhibiting high material density and clear ferromagnetic order, as evidenced by both macroscopic VSM and high-resolution scanning NV magnetometry. While the measured saturation magnetization is consistent with bulk nickel, the observed saturation fields (≈ 200 mT) and remanence ($\approx 11\%$ in VSM measurements) point toward pronounced domain-wall pinning. Furthermore, the absence of significant magnetic domain contrast at sub-micrometer distances during the scanning NV magnetometry characterization in the structure's remanent state suggests a fragmented domain state with a high degree of magnetic flux closure.

This work demonstrates that sTTA-UC-

driven photochemistry is a powerful and versatile tool for additive manufacturing of functional metallic microstructures. The presented concept provides a promising route towards complex magnetic microcomponents for potential applications in microrobotics, sensing, and integrated microsystems.

Methods

Photophysical characterization

Absorption spectroscopy was carried out with a JASCO V-780 double-beam UV/vis to NIR spectrophotometer. For measurements up to 350 nm a deuterium lamp and from 350 nm to 800 nm a halogen lamp was facilitated. The luminescence spectra were recorded with a HORIBA FluoroLog3 22 τ with a 450 W Xenon lamp and double-grating monochromator units for the excitation light and emitted light by the sample. Further, luminescence lifetimes were measured by time-correlated single photon counting (TCSPC) with the HORIBA DeltaFlex using a NanoLED (pulse width <

1.3 ns) at a wavelength of 389 nm. The internal response function was recorded using suspension of LUDOX[®] in water to scatter the excitation light.

Further data evaluation

The recorded TCSPC decays were analyzed using the HORIBA DecayAnalysis software. All data were fitted using reconvolution fitting with the internal response function and a mono exponential function (Fig. S2 & S3). For evaluation of the Stern-Volmer constant K_{SV} and the quenching rate of perylene with DIPEA, the quencher concentration [Q] was plotted against the excited state lifetime τ of perylene with DIPEA and τ_0 without added quencher. The data were fitted according to the equation 2.

$$\frac{\tau}{\tau_0} = 1 + K_{SV} \quad (2)$$

To extract the quenching rate k_q the relation 3 was used.

$$K_{SV} = k_q \cdot \tau_0 \quad (3)$$

Preparation of the photoresist

The resist is prepared under ambient conditions. The final resist contains 10 mM perylene, 100 μ M Erythrosine B, 1 mM $\text{NiCl}_2 \cdot 6\text{H}_2\text{O}$ and 574 mM DIPEA in DMI.

DMI (>99%) and perylene (>98%) were purchased from Tokyo Chemical Industry Co., Ltd. (TCI, Tokyo, Japan). $\text{NiCl}_2 \cdot 6\text{H}_2\text{O}$ (>98%) was purchased from VWR International, LLC (Radnor, PA, USA). DIPEA (>99% for synthesis) was purchased from Carl Roth GmbH + Co. KG (Karlsruhe, Germany) and Erythrosine B was purchased from ClinTech Limited (Manchester, UK). All chemicals are used as bought.

DLW setup

For DLW, a self built setup is used. The laser is a continuous wave diode-pumped solid-state Neodymium Vanadate (Nd:YVO_4) with a wavelength of 532 nm and an average power of up to 2.2 W (Coherent Verdi V-2). The laser light is

focused onto the substrate with a NA 1.4 oil immersion objective. Scanning of the laser focus is enabled by galvanometric mirrors. The laser power can be adjusted using an acousto-optical modulator. A sketch of the setup as well as further details can be found in a previous paper.³⁷

To test the theory if the proposed process could be assisted by additionally trapping generated particles by enhancement of their near field *via* localized surface plasmon resonance induced by 2PA like Wang *et al.* did,²¹ a 780 nm laser with 150 fs pulses and a repetition rate of 80 MHz with an average power of up to 1.5 W was added to the setup. The laser foci of both lasers were aligned in the printing process. The structures printed with this setup did not show any noticeable improvement compared to the ones without the added pulsed laser.

Following a similar approach, experiments with a pulsed laser that emits a wavelength that is twice the excitation wavelength of the sensitizer were carried out to investigate the mechanism of employing a 2PA process to sensitize the sTTA-UC process. For this purpose, the compression module of a Primus series laser by Stuttgart Instruments with a fixed wavelength at 1040 nm with an average output power of 1 W at a pulse duration of 450 fs and a repetition rate of 40 MHz was employed and focused with a NA 0.5 objective into a vial containing 2 mL of the resist. The laser power corresponds to a peak power of $\sim 5.5 \times 10^4$ W. While a yellow luminescence consistent with the fluorescence of Erythrosine B at 553 nm⁴¹ was observed, no observable metal particles were formed.

Determination of the ferromagnetic characteristics of the printed structures

Vibrating sample magnetoetry (VSM) measurements were conducted using a commercial setup (PPMS DynaCool, Quantum Design) at a temperature of 300 K. The sample was glued to a quartz sample holder that oscillates inside of a pick-up coil at 40 Hz and with an amplitude of

2 mm. The induced voltage in the pick-up coil is used to determine the magnetic moment of the sample as a function of externally applied magnetic field. The magnetic field is applied via a superconducting solenoid coil around the sample and pick-up coil.

For each magnetic field setting, the average of three measurements was used to precisely determine the magnetic moment, whereas only clusters with a standard deviation of less than 2 nAm^2 were considered in the evaluation.

The volume of the sample used in the VSM measurement was obtained using a confocal microscope. After measuring the topography of the sample, the volume was evaluated using a Matlab script. By tweaking the parameter settings in the script based on the possible factors, the volume was estimated both upwards and downwards. The volume was found to be $(1.05 \pm 0.17) \times 10^{-14} \text{ m}^3$. With the determined material density of $(96 \pm 3)\%$, the magnetic volume of the sample is given by $(1.01 \pm 0.19) \times 10^{-14} \text{ m}^3$. Dividing the magnetic moment by this volume yields the magnetization.

A linear diamagnetic background, originating mainly from the quartz sample holder and substrate, was removed by calculating the mean slope and offset from linear fits within the saturated regimes $0.3 \text{ T} < |\mu_0 H_{\text{ext}}| < 1 \text{ T}$. This regime was also used to calculate the saturation magnetization by averaging across the magnetic moments of all data points within this region.

Nitrogen-vacancy magnetometry

To investigate the magnetic properties of single structures, we employ Nitrogen-vacancy magnetometry. Nitrogen-vacancy (NV) centers in diamond are point defects consisting of a substitutional nitrogen atom adjacent to a carbon vacancy. Their electronic ground state is a spin triplet that can be initialized and read out optically and is coherently manipulated with microwaves, which enables quantitative magnetometry under ambient conditions.⁴² In an external magnetic field, the degeneracy of the $m_s = \pm 1$ spin states is lifted and the corresponding optically detected magnetic resonance

(ODMR) frequencies f_- and f_+ are Zeeman shifted. From the splitting between these resonances, the projection of the local magnetic field onto the NV quantization axis, $\mu_0 H_{\text{NV}\parallel}$, can be extracted using the NV gyromagnetic ratio, providing a direct measure of the stray field above the sample.

For the measurements, a commercial scanning NV setup (ProteusQ, Qnami) is operated in frequency modulated (FM) atomic force microscopy (AFM) mode, with a single NV center at the apex of a diamond tip (MX+ series, (100)-oriented). The NV center is excited with a 515 nm laser focused onto the tip through a microscope objective (NA = 0.7), and the resulting fluorescence is detected while applying a microwave field of frequency f_{MW} to record the ODMR spectra (Fig. 5b).

Acknowledgement This work was funded by the Deutsche Forschungsgemeinschaft (DFG, German Research Foundation) under project number TRR 173-268565370, Spin+X (Project A12) and project number 172116086 - SFB 926 (project B11). One of the laser systems (Stuttgart Instruments) used for this study has been funded by the Deutsche Forschungsgemeinschaft (DFG, German Research Foundation) – project number 459322035. We acknowledge the use of our Scanning NV Magnetometer, funded by the Deutsche Forschungsgemeinschaft (DFG, German Research Foundation) - 491229782 within the major instrumentation initiative “Spin-based quantum light microscopy (SQLM)”. We acknowledge support from nano structuring center (NSC) at the RPTU and thank especially Dr. Thomas Löber for preparing the focused ion beam cross-sections. K. Rediger gratefully acknowledges the financial support by the Fonds der Chemischen Industrie (FCI, 115571) in the form of a Kekulé scholarship and thanks Prof. Dr. Maria Wächtler (Christian-Albrechts-Universität zu Kiel) for her continuous and fruitful support.

Supporting Information Available

The following files are available free of charge.

- Supplementary information: A PDF containing figures with more detailed measurement data (spectroscopic data of the resist, EDX obtained countmaps of a nickel structure) and simulated data (modeling of the magnetic stray field for a nickel structure).

References

1. Schuller, J. A.; Barnard, E. S.; Cai, W.; Jun, Y. C.; White, J. S.; Brongersma, M. L. Plasmonics for Extreme Light Concentration and Manipulation. *Nat. Mater.* **2010**, *9*, 193–204.
2. Yang, K.-Y.; Verre, R.; Butet, J.; Yan, C.; Antosiewicz, T. J.; Käll, M.; Martin, O. J. Wavevector-Selective Nonlinear Plasmonic Metasurfaces. *Nano Lett.* **2017**, *17*, 5258–5263.
3. Anker, J. N.; Hall, W. P.; Lyandres, O.; Shah, N. C.; Zhao, J.; Van Duyne, R. P. Biosensing with Plasmonic Nanosensors. *Nat. Mater.* **2008**, *7*, 442–453.
4. Hu, Y.; Kumar, P.; Xu, R.; Zhao, K.; Cheng, G. J. Ultrafast Direct Fabrication of Flexible Substrate-Supported Designer Plasmonic Nanoarrays. *Nanoscale* **2016**, *8*, 172–182.
5. Gibson, I.; Rosen, D.; Stucker, B.; Khorasani, M. *Additive Manufacturing Technologies*, 3rd ed.; Springer: Cham, 2021.
6. Thompson, M. K.; Moroni, G.; Vaneker, T.; Fadel, G.; Campbell, R. I.; Gibson, I.; Bernard, A.; Schulz, J.; Graf, P.; Ahuja, B.; others Design for Additive Manufacturing: Trends, Opportunities, Considerations, and Constraints. *CIRP Ann.* **2016**, *65*, 737–760.
7. Otuka, A. J. G.; Tomazio, N. B.; Paula, K. T.; Mendonça, C. R. Two-Photon Polymerization: Functionalized Microstructures, Micro-Resonators, and Bio-Scaffolds. *Polymers* **2021**, *13*, 1994.
8. Soto, F.; Wang, J.; Ahmed, R.; Demirci, U. Medical Micro/Nanorobots in Precision Medicine. *Adv. Sci.* **2020**, *7*, 2002203.
9. Maruo, S.; Nakamura, O.; Kawata, S. Three-Dimensional Microfabrication with Two-Photon-Absorbed Photopolymerization. *Opt. Lett.* **1997**, *22*, 132–134.
10. Skliutas, E.; Merkininkaitė, G.; Maruo, S.; Zhang, W.; Chen, W.; Deng, W.; Greer, J.; Freymann, G. v.; Malinauskas, M. Multiphoton 3D Lithography. *Nat. Rev. Methods Primers* **2025**, *5*, 15.
11. Tanaka, T.; Ishikawa, A.; Kawata, S. Two-Photon-Induced Reduction of Metal Ions for Fabricating Three-Dimensional Electrically Conductive Metallic Microstructure. *Appl. Phys. Lett.* **2006**, *88*.
12. Blasco, E.; Müller, J.; Müller, P.; Trouillet, V.; Schön, M.; Scherer, T.; Barner-Kowollik, C.; Wegener, M. Fabrication of Conductive 3D Gold-Containing Microstructures via Direct Laser Writing. *Adv. Mater.* **2016**, *28*, 3592–3595.
13. Waller, E. H.; Karst, J.; von Freymann, G. Photosensitive Material Enabling Direct Fabrication of Filigree 3D Silver Microstructures via Laser-Induced Photoreduction. *Light: Advanced Manufacturing* **2021**, *2*, 228–233.
14. Zhang, N.; Wang, Z.; Zhao, Z.; Zhang, D.; Feng, J.; Yu, L.; Lin, Z.; Guo, Q.; Huang, J.; Mao, J.; others 3D Printing of Micro-Nano Devices and their Applications. *Microsyst. Nanoeng.* **2025**, *11*, 35.
15. Zhang, W.; Li, G.; Luan, X.; Liu, F. From Biohybrid Actuators To Smart Manufacturing: Advancing Microrobots for Minimally Invasive Medicine. *Journal of Bionic Engineering* **2025**, 1–27.

16. Harris, D. C. *Lehrbuch der quantitativen Analyse*; Springer-Verlag: Berlin, Germany, 2014.
17. Hohmann, J. K.; Renner, M.; Waller, E. H.; von Freymann, G. Three-Dimensional μ -Printing: An Enabling Technology. *Adv. Opt. Mater.* **2015**, *3*, 1488–1507.
18. Hahn, V.; Messer, T.; Bojanowski, N. M.; Curticean, E. R.; Wacker, I.; Schröder, R. R.; Blasco, E.; Wegener, M. Two-Step Absorption Instead of Two-Photon Absorption in 3D Nanoprinting. *Nat. Photonics* **2021**, *15*, 932–938.
19. Awwad, N.; Bui, A. T.; Danilov, E. O.; Castellano, F. N. Visible-Light-Initiated Free-Radical Polymerization by Homomolecular Triplet-Triplet Annihilation. *Chem* **2020**, *6*, 3071–3085.
20. Wang, Z.; Zhang, Y.; Su, Y.; Zhang, C.; Wang, C. Three-Dimensional Direct-Writing via Photopolymerization Based on Triplet–Triplet Annihilation. *Sci. China:Chem.* **2022**, *65*, 2283–2289.
21. Wang, Y.; Yi, C.; Tian, W.; Liu, F.; Cheng, G. J. Free-Space Direct Nanoscale 3D Printing of Metals and Alloys Enabled by Two-Photon Decomposition and Ultrafast Optical Trapping. *Nat. Mater.* **2024**, *23*, 1645–1653.
22. Balushev, S.; Katta, K.; Avlasevich, Y.; Landfester, K. Annihilation Upconversion in Nanoconfinement: Solving the Oxygen Quenching Problem. *Mater. Horiz.* **2016**, *3*, 478–486.
23. Huang, L.; Wu, W.; Li, Y.; Huang, K.; Zeng, L.; Lin, W.; Han, G. Highly Effective Near-Infrared Activating Triplet–Triplet Annihilation Upconversion for Photoredox Catalysis. *J. Am. Chem. Soc.* **2020**, *142*, 18460–18470.
24. Edhborg, F.; Olesund, A.; Albinsson, B. Best Practice in Determining Key Photophysical Parameters in Triplet–Triplet Annihilation Photon Upconversion. *Photochem. Photobiol. Sci.* **2022**, *21*, 1143–1158.
25. Simon, Y. C.; Weder, C. Low-Power Photon Upconversion Through Triplet–Triplet Annihilation in Polymers. *J. Mater. Chem.* **2012**, *22*, 20817–20830.
26. Yanai, N.; Kimizuka, N. Recent Emergence of Photon Upconversion Based on Triplet Energy Migration in Molecular Assemblies. *Chem. Commun.* **2016**, *52*, 5354–5370.
27. Wan, S.; Lin, J.; Su, H.; Dai, J.; Lu, W. Photochemically Deoxygenating Solvents for Triplet–Triplet Annihilation Photon Upconversion Operating in Air. *Chem. Commun.* **2018**, *54*, 3907–3910.
28. Lutkus, L. V.; Rickenbach, S. S.; McCormick, T. M. Singlet Oxygen Quantum Yields Determined by Oxygen Consumption. *J. Photochem. Photobiol., A* **2019**, *378*, 131–135.
29. Jiang, Y.; Fu, Y.; Xu, X.; Guo, X.; Wang, F.; Xu, X.; Huang, Y.-W.; Shi, J.; Shen, C. Production of Singlet Oxygen from Photosensitizer Erythrosine for Facile Inactivation of Coronavirus on Mask. *Environment International* **2023**, *177*, 107994.
30. Bennison, M. J.; Collins, A. R.; Zhang, B.; Evans, R. C. Organic Polymer Hosts for Triplet–Triplet Annihilation Upconversion Systems. *Macromol.* **2021**, *54*, 5287–5303.
31. Tran, J.; Olmsted III, J. Intramolecular Triplet-Triplet Energy Transfer from Xanthene Dyes to an Anthryl Substituent. *J. Photochem. Photobiol., A* **1993**, *71*, 45–49.
32. Wu, W.; Zhao, J.; Sun, J.; Guo, S. Light-Harvesting Fullerene Dyads As Organic Triplet Photosensitizers for Triplet–Triplet Annihilation Upconversions. *J. Org. Chem.* **2012**, *77*, 5305–5312.
33. Romero, N. A.; Nicewicz, D. A. Organic Photoredox Catalysis. *Chem. Rev.* **2016**, *116*, 10075–10166.

34. Montalti, M.; Credi, A.; Prodi, L.; Gandolfi, M. T. *Handbook of Photochemistry*; CRC Press: Boca Raton, FL, USA, 2006.
35. Goliszewska, K.; Rybicka-Jasińska, K.; Clark, J. A.; Vullev, V. I.; Gryko, D. Photoredox Catalysis: the Reaction Mechanism Can Adjust to Electronic Properties of a Catalyst. *ACS Catal.* **2020**, *10*, 5920–5927.
36. Kramida, A. and Ralchenko, Yu. and Reader, J. and the NIST ASD Team NIST Atomic Spectra Database (version 5.12). 2024; National Institute of Standards and Technology, Gaithersburg, MD; accessed February 13, 2026, <https://physics.nist.gov/asd>.
37. Hering, J.; Waller, E. H.; Von Freymann, G. Automated Aberration Correction of Arbitrary Laser Modes in High Numerical Aperture Systems. *Opt. Express* **2016**, *24*, 28500–28508.
38. Lakowicz, J. R. *Principles of Fluorescence Spectroscopy*, 3rd ed.; Springer, 2006.
39. Sulitanu, N. Saturation Magnetization of NiW Thin Films. *J. Magn. Magn. Mater.* **1992**, *113*, 238–242.
40. Bozorth, R. M. *Ferromagnetism*, 5th ed.; D. Van Nostrand Co.: Princeton, NJ, U.S.A., 1951.
41. Cheng, Z.; Du, L.; Zhu, P.; Chen, Q.; Tan, K. An Erythrosin B-Based “Turn On” Fluorescent Sensor for Detecting Perfluorooctane Sulfonate and Perfluorooctanoic Acid in Environmental Water Samples. *Spectrochim. Acta, Part A* **2018**, *201*, 281–287.
42. Rondin, L.; Tetienne, J.-P.; Hingant, T.; Roch, J.-F.; Maletinsky, P.; Jacques, V. Magnetometry With Nitrogen-Vacancy Defects in Diamond. *Rep. Prog. Phys.* **2014**, *77*, 056503.